Title

A Magnetic Digital Microfluidic Platform for Point-of-care Diagnostics

Permalink

https://escholarship.org/uc/item/1cn5h795

Author

Yu, Wenzhuo

Publication Date

2021

Peer reviewed|Thesis/dissertation

UNIVERSITY OF CALIFORNIA

Los Angeles

A Magnetic Digital Microfluidic Platform for Point-of-care Diagnostics

A thesis submitted in partial satisfaction of the

requirements for the degree Master of Science

in Electrical and Computer Engineering

by

Wenzhuo Yu

2021

ABSTRACT OF THE THESIS

A Magnetic Digital Microfluidic Platform for Point-of-care Diagnostics

by

Wenzhuo Yu

Master of Science in Electrical and Computer Engineering

University of California, Los Angeles, 2021

Professor Sam Emaminejad, Chair

Automated technologies that can perform massively parallelized and sequential fluidic operations at small length scales can resolve major bottlenecks encountered in various fields, including medical diagnostics, -omics, drug development, and chemical/material synthesis. Inspired by the transformational impact of automated guided vehicle systems on manufacturing, warehousing, and distribution industries, here, we devise a ferrobotic system which employs a network of individually addressable robots, each performing designated micro/nano-fluid manipulation-based tasks in cooperation with other robots toward a shared objective. The underlying robotic mechanism facilitating fluidic operations is realized by addressable electromagnetic actuation of miniature mobile magnets that exert localized magnetic body forces on aqueous droplets filled with biocompatible magnetic nanoparticles. The contactless and high-strength nature of the actuation mechanism inherently renders it rapid (~10 cm/s), repeatable (> 10,000 cycles), and robust (> 24 hours). The robustness and individual addressability of ferrobots provide a foundation for the deployment of a network of ferrobots to carry out cross-collaborative logistics efficiently. These traits, together with the reconfigurability of the system, are exploited to devise and integrate passive/active advanced functional components (*e.g.*,

droplet dispensing, generation, filtering, and merging), enabling versatile system-level functionalities. By applying this ferrobotic system within the framework of a microfluidic architecture, the ferrobots were tasked to work cross-collaboratively toward the quantification of active matrix metallopeptidases (a biomarker for cancer malignancy and inflammation) in human plasma, where various functionalities converged to achieve a fully automated assay.

The thesis of Wenzhuo Yu is approved.

Dino Di Carlo

Aydogan Ozcan

Sam Emaminejad, Committee Chair

University of California, Los Angeles

2021

TABLE OF CONTENTS

LIST OF FIGURES

ACKNOWLEDGEMENTS

great cooperation, valuable comments, and wise advice in these years. I am very proud of the work we published all together.

Last my thanks would go to my beloved family for their loving considerations and great confidence in me all through these years.

Chapter 1 Introduction

1.1. From supply chain logistics to microfluidic logistics

The advent of Industry 4.0 is pioneered by automated guided vehicles (AGV) that are widely used in distribution and supply chain logistics to perform autonomous, accurate, and consistent cargo transportation, while reducing transit times and labor costs [1]. The flexibility and scalability of such mobile automated systems, in conjunction with their ability to assign specific tasks to individual vehicles cooperating in a large network, provide new degrees of automation in comparison to physically constrained conveyor-belt or forklift-operated systems [2]. The same degrees of automation are poised to revolutionize applications such as medical diagnostics [3,4], -omics [5-7], drug development [8], and chemical/material synthesis [9]. In that regard, the full potential of these applications can be unlocked by adopting solutions centering on microfluidic logistics, herein defined as the detailed coordination of diverse, large-scale, and small-volume fluid handling operations to perform a plethora of sample processing and analysis tasks.

To this end, conventional continuous-flow microfluidic systems have shown high throughput and robust fluid handling capabilities [10-12]. However, their predefined fluid pathways and geometrically constrained operations severely limit their adaptability and automation, imposing the same limitations as conveyor-belt systems within larger-scale settings. Aiming to resolve such constraints, digital microfluidic actuation techniques such as electrowetting-on-dielectric (EWOD) have emerged, capable of transporting discrete droplets on an open surface in a programmable fashion [13-15]. However, inherent limitations of EWOD devices, stemming from the reliance on direct interactions between the solution and the electrified surfaces, can restrict their service life and compatibility with other peripheral components, thus narrowing their application diversity [16,17].

1.2. Thesis overview

Here, inspired by the transformational impact of automated guided robotic systems on the manufacturing and distribution industries, we devised a robotic system which employs a network of individually addressable robots, each performing designated micro/nano-fluid manipulation-based tasks in cooperation with other robots. As illustrated in Fig. 1.1a, analogous to a standard AGV system, which consists of three primary entities, including a navigation floor, an electric motor, and a cargo carrier for package delivery, our robotic system can be described as: 1) an electromagnetic navigation floor, which can be programmed to establish localized electromagnetic (EM) fields in an addressable matrix of coils; 2) a millimeter-scale permanent magnet as a motor, the movement of which is controlled by the activated EM field(s); and 3) a ferrofluid droplet carrier, encapsulating the bio/chemical sample of interest (*i.e.*, the "package"), which is set in motion upon experiencing strong body forces originating from the interaction of the ferrofluid's magnetic nanoparticle constituents with the motor's magnetic actuation field.

Effectively, the devised design leverages EM induction to achieve scalable control, and an intermediary EM-controlled permanent magnet to amplify the actuation field exerted on the ferrofluid (Fig. 1.1B). In this way, we overcome the fundamental limitations of previously reported magnetic digital microfluidics, which use complex translational stages and bulky magnets that are not portable [18,19] or electromagnetic coils [20,21] that lack the ample driving forces to execute efficient fluid operations. The addressability and strength of the ferrofluid actuation enables new degrees of mobility and automation central to the devised robotic system; hereafter, referred to as "ferrobotic system".

The contactless and high-strength nature of the ferrobotic actuation mechanism inherently renders it rapid, repeatable and robust. These traits, together with the reconfigurability of the

2

ferrobotic system, can be exploited to integrate passive and active functional components to implement advanced and diverse microfluidic operations (*e.g.*, droplet dispensing, generation, merging, filtering) besides basic transportation operations (Fig. 1.1C). Depending on the objective at hand, a set of these operations can be combined within a disposable microfluidic architecture to deliver versatile system-level microfluidic functionalities.

This high degree of robustness and the individual addressability of ferrobots can be in turn leveraged to deploy a network of ferrobots that carry out generalizable cross-collaborative objectives, centering on microfluidic logistics, such as fluidic package sorting. To illustrate the utility of the ferrobotic system in diverse application spaces, this system was specifically applied to execute a set of cross-collaborative and diverse operations, toward the quantification of active matrix metallopeptidases (MMP, a biomarker for cancer malignancy and inflammation) in human plasma [22-24], where its reconfigurable functionality and teamwork capability converged to implement a fully automated assay.
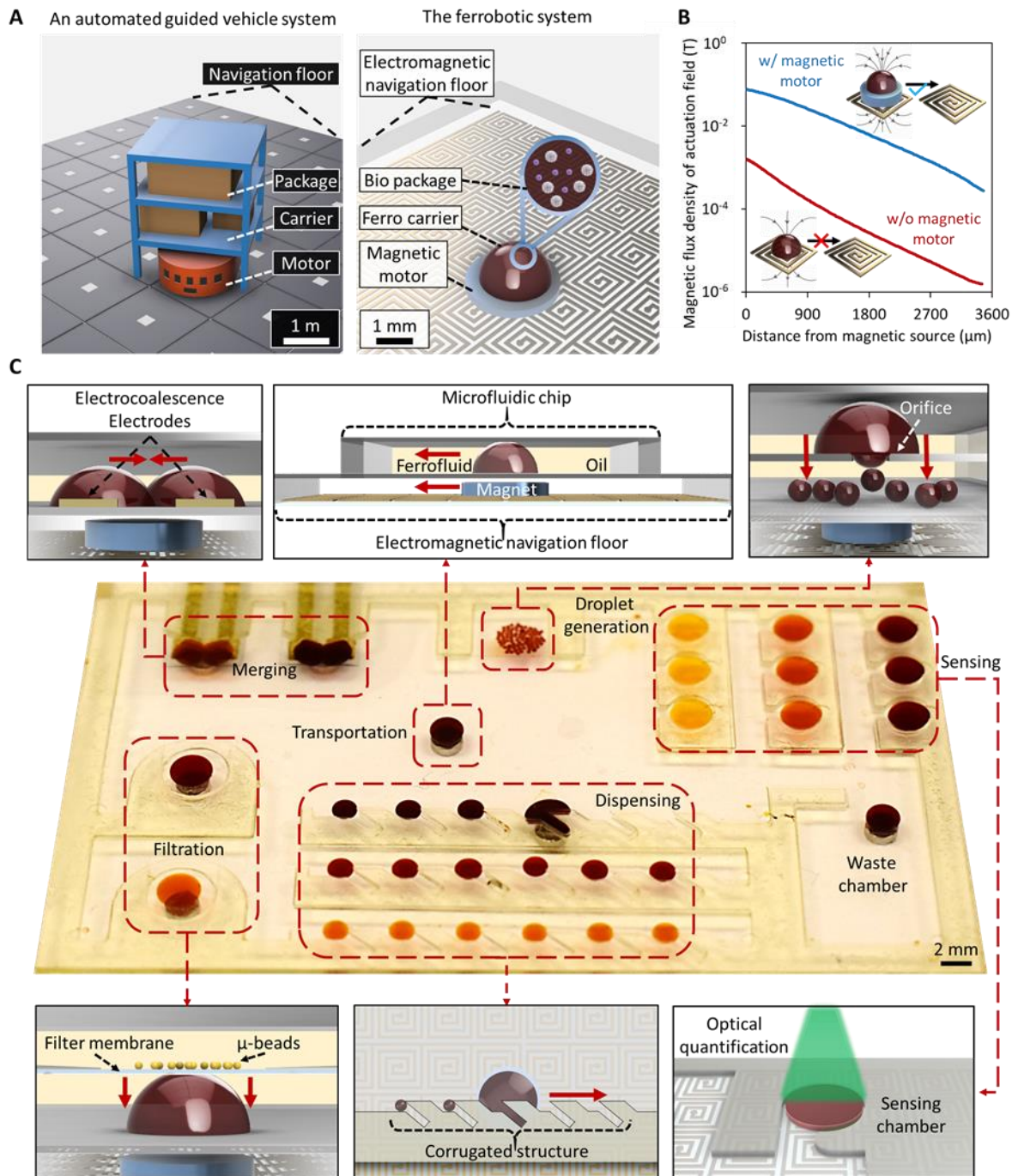
Figure 1.1 *The overview of ferrobotic system concept and mechanism. a) An analogy: mobility and automation in an AGV system and the devised ferrobotic system; b) Simulation results depicting the amplification of the actuation capability with the magnetic motor (the x-axis is the vertical distance from the center of the magnetic source); c) Optical image of a representative multifunctional ferrobotic system capable of performing diverse operations, including droplet package transportation, merging, generation, filtration, dispensing, and sensing. Rendered images of the droplets are for illustration purposes only (droplets can form hemisphere or disk-like shapes depending on the channel geometry).*

4

Chapter 2 Amplified addressable electromagnetic actuation

2.1. Design of the navigation floor

By utilizing the electromagnetic coil matrix as the addressable actuator, and the millimeter-scale permanent magnet as the magnetic field actuation amplifier, robust ferrobotic fluid operations can be realized within a compact footprint. As seen in the magnetic field simulation results, illustrated in Fig. 1.1B and Fig. 2.1, the incorporated permanent magnet amplifies the actuation magnetic field by approximately two orders of magnitude (generated from passing of a 0.2 A DC current through the electromagnetic coil). In this way, high force actuation of relatively dilute magnetic solutions and/or smaller fluid volumes is achieved, rendering robust fluid transportation. Fluid transportation is the ferrobotic system's core functionality where an encapsulated package within the ferrofluidic carrier can be directed by the sequential activation of the EM coils along a desired route on the navigation floor.
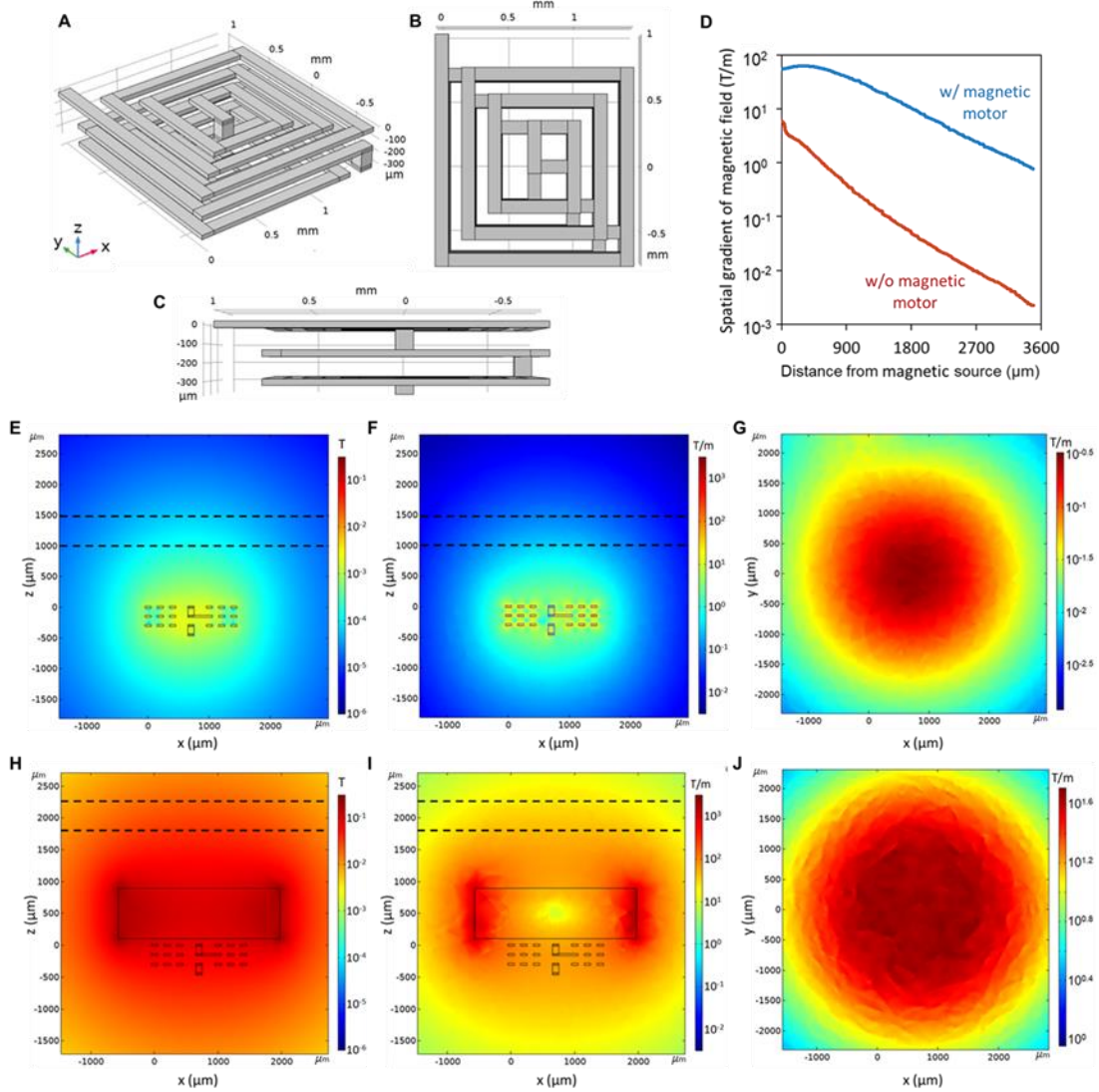
Figure 2.1 *EM-coil geometry and magnetic field simulation. Oblique (a), top (b) and side (c) view of the EM-coil's geometry; d) COMSOL simulation results of the spatial gradient of the magnetic field with and without the magnetic motor (i.e., the ferrobot). The x-axis is the distance from the magnetic source center along the z-axis; e,f) magnetic field intensity (e) and spatial gradient of the magnetic field (f) in x-z plane in the absence of the ferrobot. The dashed lines outline the boundaries of the microfluidic chamber; g) spatial gradient of the magnetic field in x-y plane (1 mm above the coil) in the absence of the ferrobot; h,i) magnetic field intensity (H) and spatial gradient of the magnetic field (I) in x-z plane in the presence of the ferrobot. The dashed lines outline the boundaries of the microfluidic chamber; j) spatial gradient of the magnetic field in the x-y plane (1 mm above the coil) in the presence of the ferrobot.*

The navigation floor was fabricated on a multi-layer printed circuit board (PCB), which at its

core is comprised of a 32 × 32 EM coil matrix, where each element is realized as a 3-layered

6

spiral structure (Fig. 2.1). The multi-layer implementation allows the proportional increase of the localized EM induction capability of each element for ferrobot attraction. To activate these elements in an addressable manner, two integrated circuit (IC) switches were incorporated in the PCB for row and column selection (Fig. 2.2), which are connected to external power sources and controlled by a microcontroller unit (MCU).
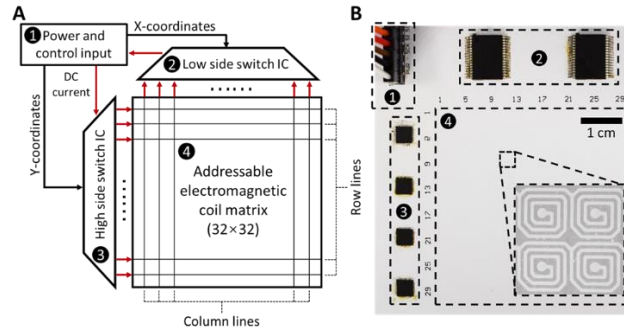
Figure 2.2 *Design and characterization of the navigation floor for package transportation. a) Schematic diagram of the control circuitry; b) Optical image of the implemented control circuitry and the navigation floor with the close-up view of four neighboring EM coils;*

Depending on the task at hand, and by programming at the MCU level, these coils can be sequentially and/or simultaneously activated to engineer the desired paths for a single or multiple ferrobot(s). To illustrate this feature, we programmed the MCU to navigate single ferrobots through U-, C-, L-, and A-like routes, as well as four ferrobots to simultaneously trace the perimeter of a square-like route (Fig. 2.3). In all scenarios, the ferrobots successfully carried their designated loads.
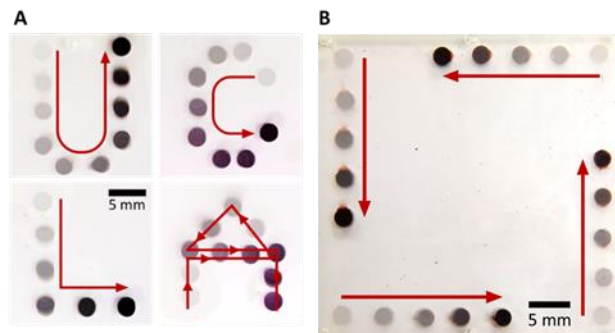
Figure 2.3 Single- and multi-ferrobot transportation. Overlaid sequential images visualize the commuted path of the ferrobot. a) ferrobots are programmed with different navigation plans, the duration for commuting "U", "C", "L" and "A" paths were correspondingly 1.4 s, 1.4 s, 0.7 s, and 2.3 s. b) four ferrobots are programmed to commute simultaneously (duration: 7 s).

2.2. Characterization of transportation

As shown in Fig. 2.4, with the devised approach, maximum droplet transportation velocities on the order of 10 cm/s can be achieved. The maximum velocity of the droplet initially increases along with its size, showing the dominance of the driving magnetic force on relatively small droplets. The following decrease in maximum velocity illustrates the increased dominance of frictional forces beyond a certain droplet size (for an expanded discussion on this topic, please refer to Supplementary Information). The same trend is observed for a more diluted ferrofluid concentration (50% dilution by volume, also shown in Fig. 2.4). Here, the droplet volume characterization range is chosen based on the envisioned microfluidic droplet applications (*e.g.*, the MMP assay).
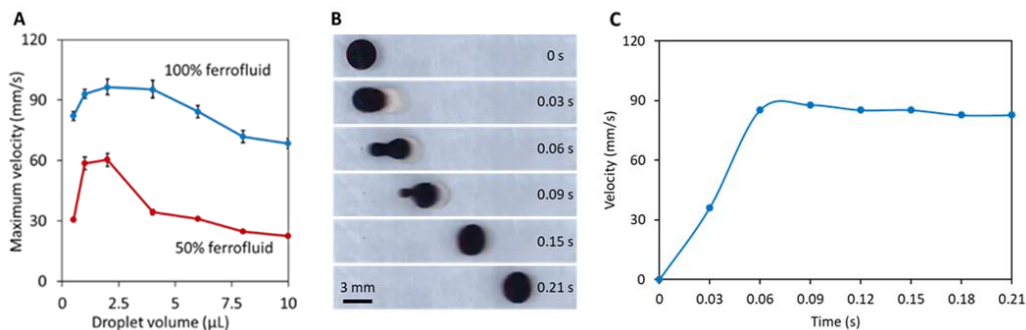
Figure 2.4 Characterization of the transportation. a) Characterization of the maximum transportation velocity for two different ferrofluid concentrations. Error bars indicate standard error (n = 3). b) Sequential imaging of a representative droplet moving along the navigation floor. c) Corresponding measured averaged velocity.

2.3. Characterization of actuation robustness

The contactless aspect of the actuation mechanism (*i.e.*, no ferrobotic surface interaction with the package or the surrounding fluid) inherently renders it repeatable and durable, in contrast with contact-based EWOD actuation that is susceptible to surface degradation [16, 17, 25, 26]. To demonstrate the durability of our ferrobotic system, an illustrative continuous characterization experiment was performed, which involved a 10,000-cycle automated oscillatory transport (frequency: 0.1 Hz) of a package over the duration of > 24 hours (Fig. 2.5a). Specifically, the ferrobot was programmed to automatically move in and out of contact with an impedance sensing electrode pair (Fig. 2.6a), patterned on the substrate of a microfluidic chip. The electrodes were used to continuously track the entrance/departure of the package through monitoring the impedance signal change (correspondingly leading to an increased/decreased measured impedance, annotated in green/red, Fig. 2.5a). Fast Fourier Transform (FFT) analysis of the continuously recorded data (Fig. 2.5b) yielded an output fundamental frequency of 0.100 Hz, which matches the input actuation frequency at the MCU level. Furthermore, the detailed FFT analysis of the 2000 s-segmented time windows yielded less than 0.01% variation in the motion frequency of the package. We also performed oscillatory droplet transport experiments at 1 Hz with water- and plasma-based droplets (over 1000 cycles). The FFT analysis, shown in Fig. 2.6b&c, indicates that repeatable oscillatory motions are achieved for both droplet samples. It is worth noting that beyond ~10 Hz, the droplet cannot be effectively manipulated because this leads to a velocity that exceeds the maximum velocity threshold.
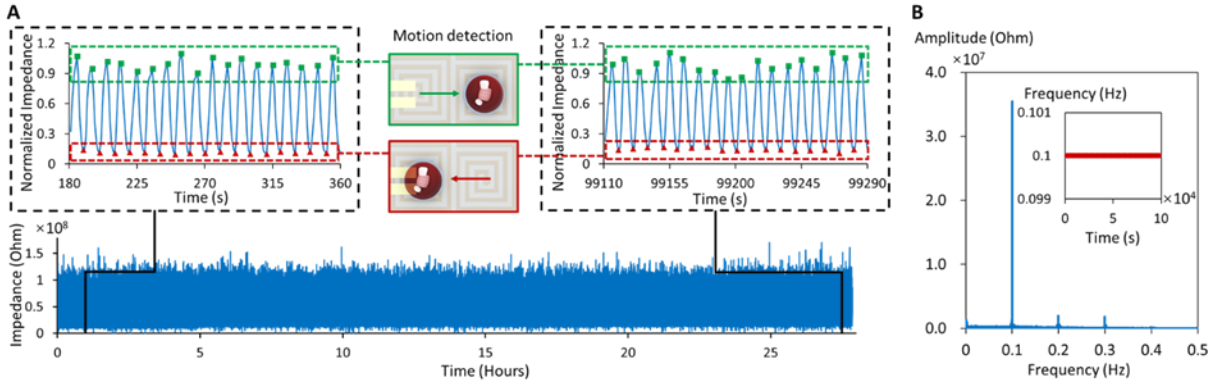
Figure 2.5 *Characterization of actuation robustness. a) Characterization of the oscillatory transportation of a package with a ferrobot (sensed with an impedance sensing electrode pair) to evaluate the robustness of the ferrobotic actuation (performed for > 24 hours); b) FFT analysis of the oscillatory profile measured by the impedance sensing electrodes in part (e). Inset shows variation of the fundamental frequency of the 2000 s-segmented time windows, depicting near zero variation.*
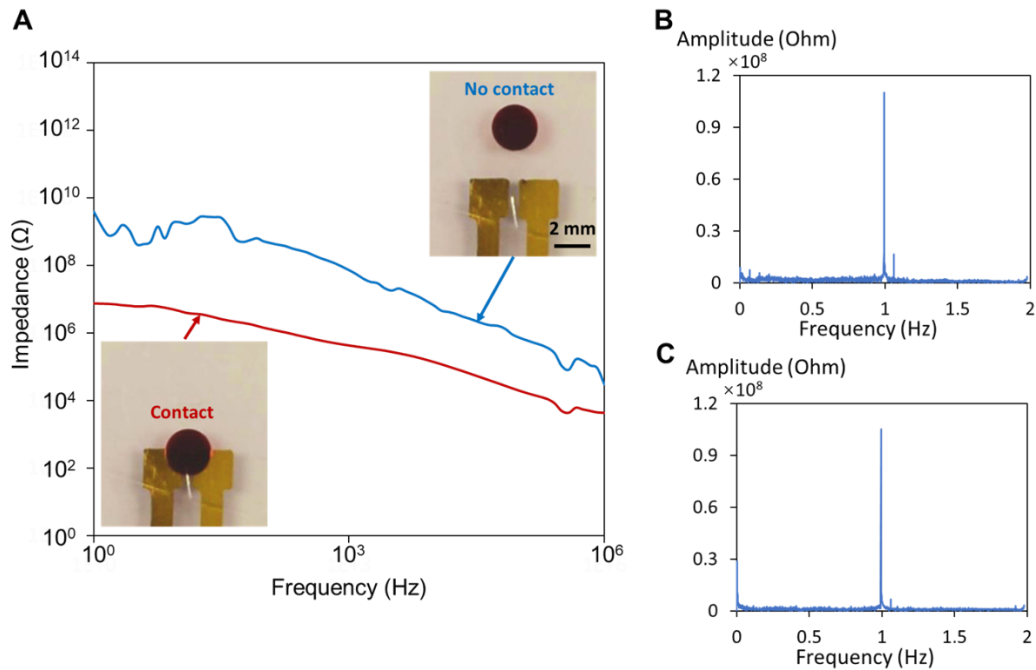
Figure 2.6 *Impedance spectrum measured by the impedance sensing electrode pair. a) The impedance spectrum shows distinct impedance differences when the ferrobot is present vs. not present (inset shows the droplet position with respect to the sensing electrodes for the corresponding measurements); b,c) Corresponding FFT of the impedance measurements tracking the oscillatory motion (1 Hz, over 1000 cycles) of the droplet with compositions: (b) 50% ferrofluid (diluted in water) and (c) 50% ferrofluid (diluted in plasma).*

10

Chapter 3 Functional components for advanced operations

3.1. Overview of functional components for advanced operations

The high-strength and contactless aspects of the devised actuation mechanism can be exploited to conveniently interface the loaded package with different passive and active peripheral components and microfluidic structures in all three spatial dimensions, thus enabling operations of interest in a reconfigurable manner. For example, by carrying the package against a corrugated microfluidic structure formed in the $x - y$ plane, droplet dispensing can be achieved. Moreover, by delivering the droplet package within a multi-layered chamber, and through VIA (vertical interconnect access) and membranes along a z axis, droplet generation and filtering can be realized. Furthermore, without causing physical/field interference, droplets can be delivered to active electro-fluidic interfaces to render complementary actuation mechanisms such as electrocoalescence for droplet merging.

3.2. Dispensing

Droplet dispensing is a precise liquid-handling capability that is useful for applications such as drug discovery, quantitative biology, and chemical analysis [27,28]. To implement the dispensing of uniformly sized droplets with the ferrobotic system, a microfluidic architecture with a corrugated wall structure was utilized. As demonstrated in Fig. 3.1a, a "parent" droplet package is guided by a ferrobot underneath the microfluidic chip. When it is transported along the corrugated structure, smaller "child" droplets are dispensed. As shown in Fig. 3.1b, the parent droplet starts moving along the corrugated wall at t = 0 s. After the droplet passes the corrugated structure at t = 1 s, due to geometric pinching, a small volume of the droplet breaks away from the parent and enters the structure. The corrugated structure can be extended into an

array format to dispense multiple droplets. As shown in the final step of Fig. 3.1b, three homogenous droplets (1.63±0.09 µL) are dispensed. To study the level of control that our system has on the dispensed droplet sizes, we designed and tested various corrugated-opening widths. The results show that by increasing the corrugated-opening width, the dispensed droplet volume can be modulated from 0.5 and 4 µL (Fig 3.1c). The same trend is observed for diluted ferrofluid concentrations (10% and 50% dilutions by volume, Fig. 3.2). If larger dispensed droplet volumes are needed, a larger magnet in addition to an enlarged corrugated-opening width may be required.
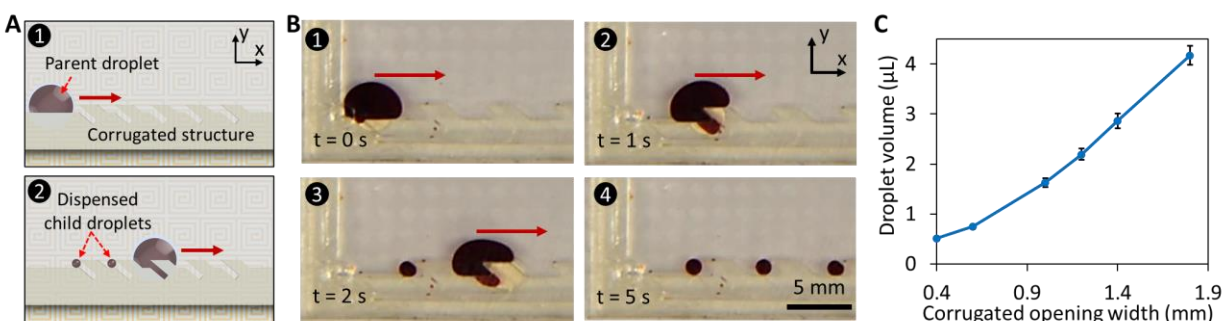
Figure 3.1 *a) Schematic illustration of the droplet dispensing mechanism, involving the transportation of the package against a corrugated microfluidic wall; b) Sequential optical images of the droplet dispensing process; c) Characterization of the dispensed droplets' size for different corrugated opening widths. Error bars indicate standard error (n = 10).*
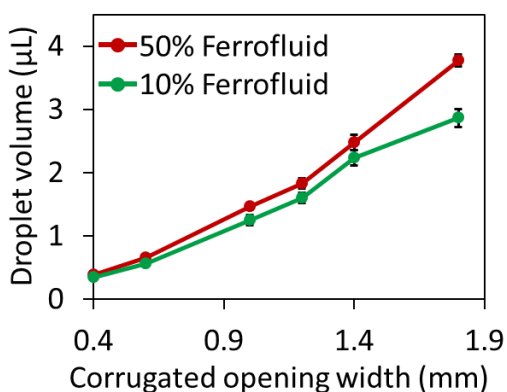
Figure 3.2 *Dispensed droplet characterization. Characterization of the dispensed droplets' size for different corrugated opening widths and using two ferrofluid concentrations. Error bars indicate standard error (n = 10).*

3.3. Generation

Furthermore, higher throughput and smaller volume droplet generation can be realized by incorporating an orifice-like VIA connecting neighboring layers in a multi-layer microfluidic architecture. As schematically illustrated in Fig. 3.3a, when the parent droplet is guided through the upper layer to the top of the orifice, it is attracted towards the lower layer by the vertically exerted magnetic force from the ferrobot. Every time a critical volume of the droplet passes the orifice, it breaks off into a child droplet. As shown in Fig. 3.3b, the following sequential events occur: 1) the transport of the parent droplet (in the upper layer) to an orifice; 2) the positioning of the parent droplet on the orifice to generate child droplets; and 3) the departure of the parent droplet, leaving behind the generated child droplets (in the lower layer). By adjusting the width of the junction orifice, the droplet volume (~10-125 nL) and the generation rate can be tuned (Fig. 3.3c, Fig. 3.4). Such nL-generated droplets can also be further manipulated by the ferrobot (Fig. 3.5).
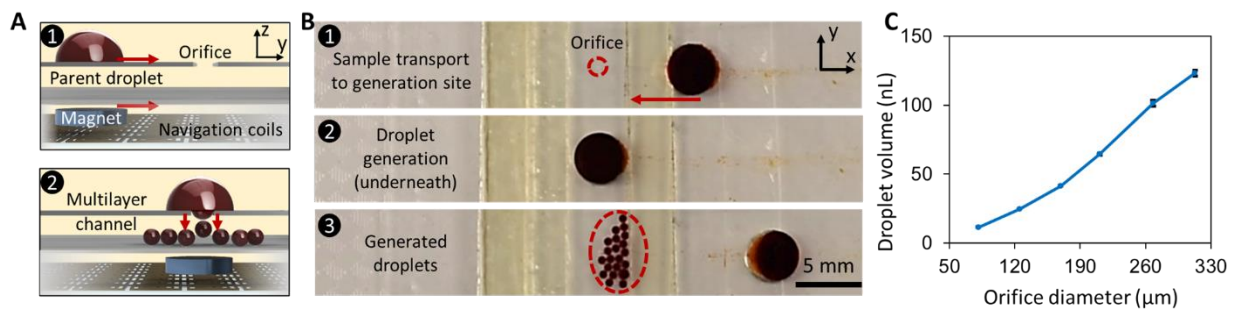
Figure 3.3 *a) Schematic illustration of the droplet generation process, involving the droplet transportation to a VIA-like orifice; b) Sequential optical images of the droplet generation process; c) Characterization of the generated droplets' volume for different orifice diameters. Error bars indicate standard error (n = 20).*
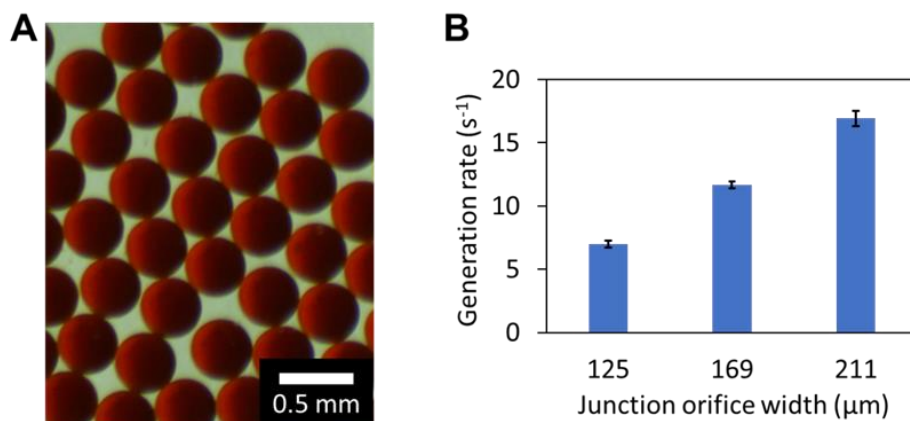
Figure 3.4 *Droplet generation characterization. a) Optical microscopic images of generated droplets using 169 µm-diameter orifice; b) Characterization of droplet generation rate for varying orifice diameters (based on counting the generated droplets over 4 s).*
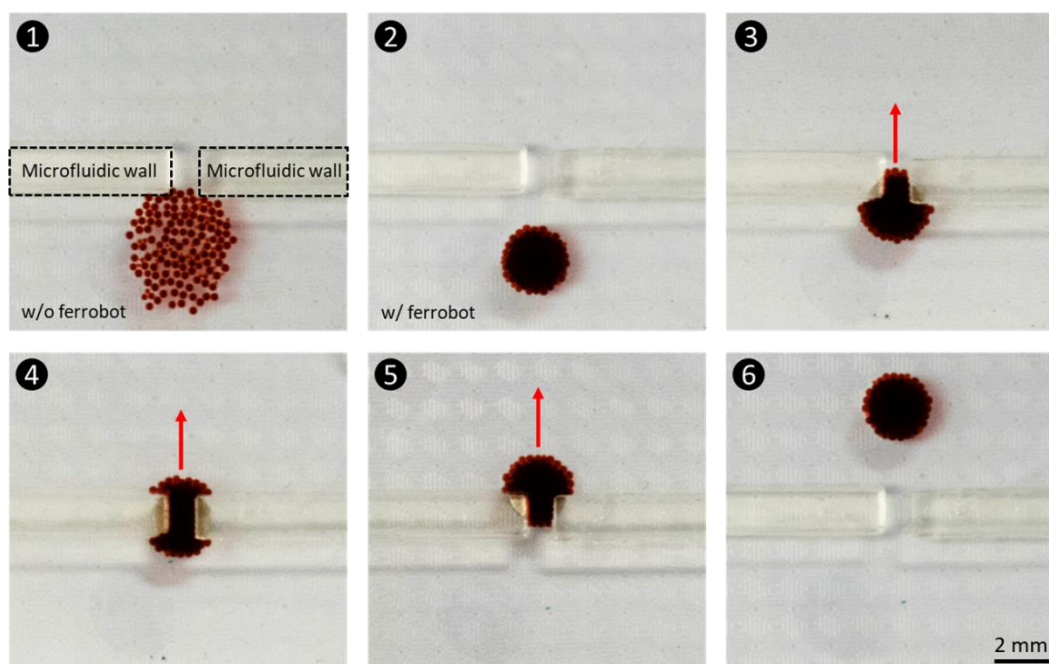
Figure 3.5 *Collective transportation of nL-droplets by a ferrobot. Sequential imaging indicates the collection and transportation of generated nL-droplets by a ferrobot through a 2 mm-wide × 1mm-long pore.*

3.4. Filtration

Microfluidic filtration is one of the key sample processing procedures required for applications such as cell separation [29,30]. Here, by incorporating a membrane between the two layers of the

microfluidic device, size-based filtration is realized. As schematically shown in Fig. 3.6a, the contactless magnetic force exerted by the ferrobot causes the droplet to be pulled through the filter to the lower layer, leaving behind particles that are too large to pass through. Specifically, here, a membrane with a size cut-off of 10-µm is used to filter out µ-beads of 25 µm diameter. To quantify the filtration capability, the ferrofluid droplet is optically imaged before and after the filtration procedure. As can be seen from Fig. 3.6b, 25 µm µ-beads can be observed in the droplet prior to filtration, and are subsequently filtered out, as evident from the post-filtration optical analysis results (three trials, Fig. 3.6c).
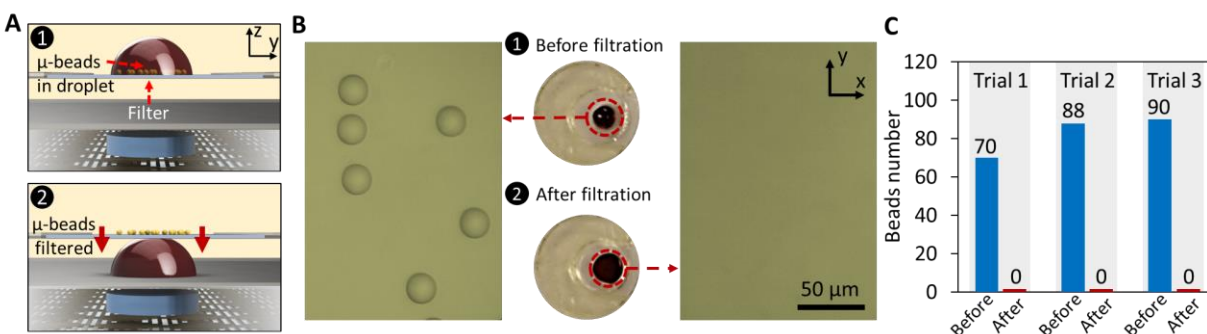
Figure 3.6 *a) Schematic illustration of the filtration mechanism; b) Optical image of the solution sample before and after filtration; c) Bead counts before and after filtration (three trials).*

3.5. Merging and mixing

Droplet merging allows for timed and metered addition of reagents and can play a critical role in performing droplet-based biological assays, aiming to measure DNA/RNA, protein, and cell properties in samples [31-35]. Here, to achieve the merging of droplets in the ferrobotic system, we leverage electrocoalescence as a complementary actuation mechanism which is non-interfering with the contactless ferrobotic actuation (Fig. 3.7). Accordingly, electrocoalescence is realized by applying 2 V across a pair of gold electrodes (2 mm × 2 mm, spaced 1 mm apart,

patterned on the substrate of the microfluidic device). Figure 3.7b show that upon applying 2 V, two droplets delivered in the vicinity of the electrodes coalesce. To achieve homogeneous and evenly distributed droplet contents after merging, chaotic fluid motion within the merged droplet can be induced by actuating neighboring electromagnetic coils with a frequency of 10 Hz in a cyclic fashion, resulting in an oscillatory motion of the ferrobot within the confines of the coil's coordinates. This cyclic motion creates folding flows in alternating directions to effectively render mixing. Figure 3.7b visually demonstrates the significant effect of the devised active mixing on shortening the time required to achieve homogeneity in a merged droplet. To quantify this effect, optical analysis on the merged red/green droplet is performed by defining a mixing index. The results are illustrated in Fig. 3.7c, demonstrating that a near-homogenous profile is achieved within ~15 s using active mixing, which is substantially shorter than without active mixing.
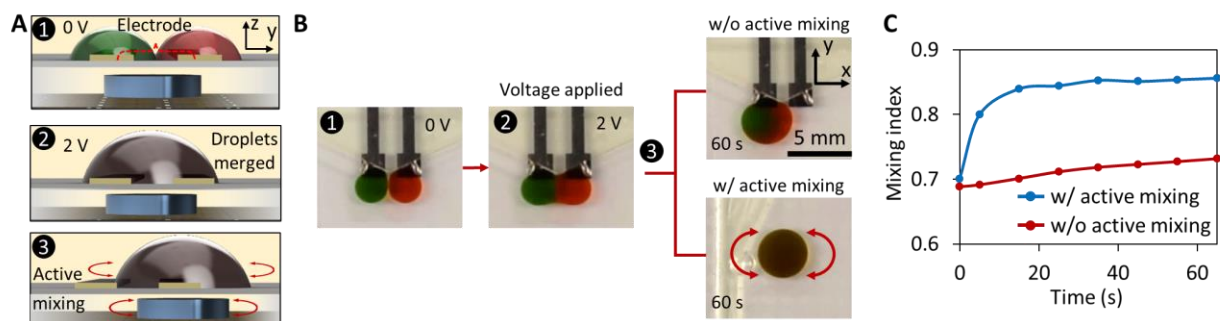
Figure 3.7 *a) Schematic illustration of droplet merging and mixing mechanisms; b) Optical images to visualize the droplet merging (upon applying 2 V) and mixing process (with and without active mixing); c) Comparison of the progressive mixing index for the two cases of with and without active mixing.*

Chapter 4 Achievement of objectives with a cross-collaborative network of ferrobots

The robustness and addressability of the ferrobotic system can be leveraged to deploy fleets of ferrobots to dynamically accomplish collaborative tasks in parallel, toward the more efficient achievement of a common objective. Here, as an example, a package-sorting mission is assigned to the ferrobotic system, where the objective is to sort randomly-sequenced packages into a sorted sequence of increasing droplet volumes. Fig. 4.1a illustrates the system-level view of the sorting procedure, which includes: 1) loading of multiple packages of various sizes into the ferrobotic system with random relative positions; 2) top-view image acquisition of the packages on the navigation floor to identify the package sizes and positions; 3) computationally deriving the navigation plan to formulate the detailed tasks for the ferrobots in accordance to the "merge sort" algorithm [36] and the acquired size and position information; and 4) communicating the corresponding assigned tasks for each of the ferrobots with the aid of the on-board microcontroller, to achieve the overarching sorting objective.

To particularly demonstrate the degree of efficiency that can be attained when deploying a cross-collaborative network of ferrobots, the n-package sorting performance achieved by a team of n ferrobots was compared against that achieved by a single ferrobot on the basis of the completion time (as detailed in Fig. 4.1b&c, for an illustrative case of $n = 8$).
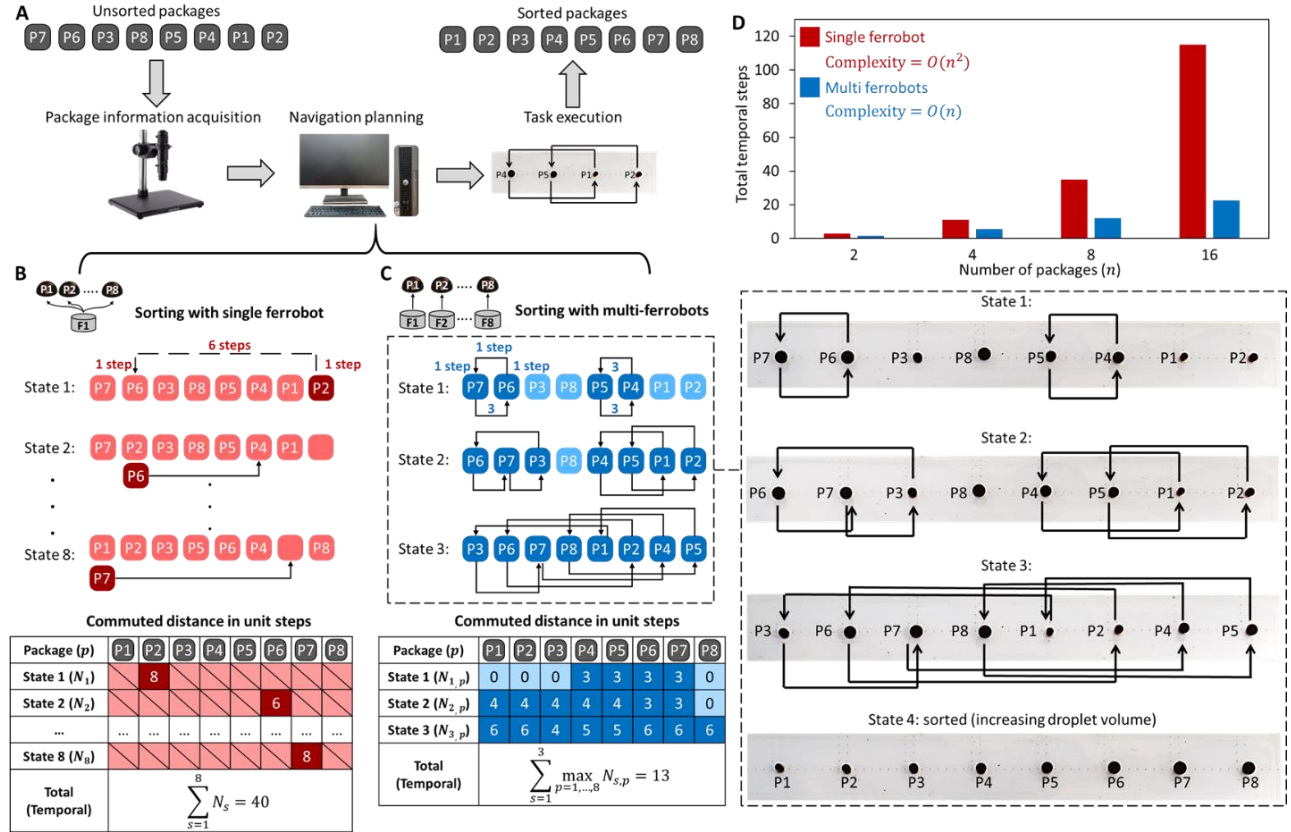
Figure 4.1 *Efficient package sorting with a cross-collaborative network of ferrobots. a)System-level view of the sorting procedure; b,c) Comparison of the sorting efficiency achieved by (b) a single ferrobot and (c) eight ferrobots tasked with sorting a random sequence of eight packages. State-by-state transitions for both scenarios are illustrated and the table details the commuted distance of each ferrobot (left). The snapshots from the sorting experiment performed with eight ferrobots are shown on the right (captured at the end of each state); d) the total temporal unit steps required for sorting 2, 4, 8, and 16 packages (based on statistical averaging of all the possible permutations).*

When only one ferrobot is used for sorting, it is responsible for the delivery of all the packages by itself. At each state (defined as the period during which the available ferrobot starts and finishes one round of package delivery), only one package can be moved to its target location. In order to quantitatively characterize the sorting efficiency, a "unit step" which equals to the distance between two navigation coils is defined to measure the distance that the ferrobots will move. For example, referring to Fig. 4.1b, at state 1, the ferrobot moves 8 unit steps (2 vertical

steps and 6 horizontal steps) to deliver package 2 ("P2") from position 8 to position 2. Since only one ferrobot is performing the task, the "temporal steps" (number of steps, which determine the maximum time elapsed over the course of a state) required to complete sorting are equal to the total unit steps moved by the single ferrobot. In the example shown, it takes the single ferrobot a total of 40 temporal steps to meet the sorting objective.

When multiple ferrobots are deployed (Fig. 4.1c), each ferrobot is charged with moving one package, and they can move in parallel with other ferrobots during the same state (following the computationally derived navigation plan in accordance with the "merge sort" algorithm, Fig. 4.2a). The corresponding experiment is visualized in Fig. 4.1c (right panel). In this scenario, the number of temporal steps for each state is determined by the maximum steps taken by a ferrobot within the team, because the ferrobots are delivering packages in parallel. For example, referring to Fig. 4.1c, in state 2, among 8 ferrobots, one ferrobot moves 0 steps, two ferrobots move 3 steps, and five ferrobots move 4 steps, yielding 4 temporal steps for that state. The total number of temporal steps to achieve the sorting objective is also equal to the sum of temporal steps for each state, which is 13 for the illustrated example. By comparison, for this illustrative example, sorting using multiple ferrobots results in about 300% increased efficiency as compared to the single ferrobot case. This degree of improvement achieved due to the deployment of a cross-collaborative network of ferrobots will be even higher for the cases requiring sorting of a larger number of packages (*i.e.*, larger n). That is because, the complexity of the mission at hand for the case of a single ferrobot increases as $O(n^2)$, while for the case of multiple ferrobots it increases linearly (*i.e.*, $O(n)$). To reinforce this point, as shown in Fig. 4.1d we derived the total temporal unit steps for the cases of $n = 2$, 4, 8, and 16, based on statistical averaging of all the possible permutations (consistent with the trend observed when simulating 10,000 randomly generated

sequences of n packages, Fig. 4.2b). Altogether, the results presented within the framework of this generalizable objective illustrate the utility of the deployment of a network of ferrobots to achieve the objective at hand efficiently as well as the suitability of the ferrobotic system for microfluidic logistics.
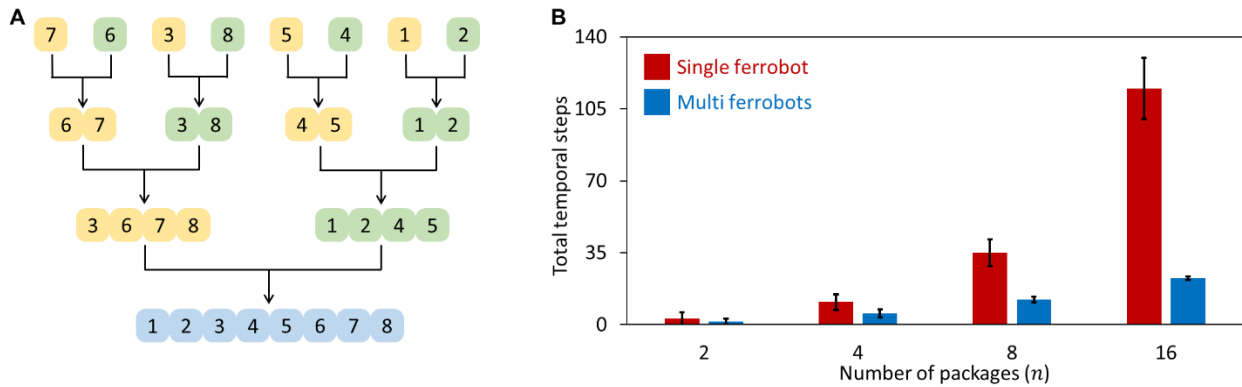
Figure 4.2 *Merge sort algorithm and sorting performance for single vs. multi ferrobots. a) Representative schematic of the application of recursive merge sort algorithm to sort an array of 8 integers; b) The averaged total temporal unit steps required for sorting n = 2, 4, 8, and 16 packages, performed with a single or n ferrobots (simulated based on 10,000 randomly generated sequence of packages for each scenario, error bars indicate standard deviation).*

Chapter 5 Application of the ferrobotic system: automated MMP bioassay

5.1. Pipelined and automated MMP assay by the ferrobotic system

Leveraging the demonstrated capability of the ferrobotic system to deliver advanced and cross-collaborative operations, we implemented a pipelined and automated bioassay equipped with a dynamic self-calibration mechanism, as an example utility of the presented technology in diverse application spaces centering on microfluidic logistics. Accordingly, the ferrobotic logistics were adapted to quantify MMP concentrations in human plasma, a biomarker extensively studied and reported as an immunological indicator, wherein the elevation of plasma MMP concentration is associated with physiological and pathological processes such as cancer metastasis [23,23,37], sepsis onset [38-40], immune activation [24, 41], and wounding healing [42,43].

Fig. 5.1a illustrates the workflow of the MMP assay, which is based on the fluorescent quantification of the enzymatic activity of MMPs from a test sample (introduced into the input well) as well as the calibrator samples, indicated by the intensity of fluorescent signals. To realize an automatic self-calibration mechanism, pre-loaded source samples (introduced at the source well array, with known concentrations of the MMP collagenase) are used for the construction of calibrator samples *in-situ*, providing optional flexibility to dynamically construct new calibrator concentrations (*e.g.*, [C_2] in Fig. 5.1a). To facilitate optical readout, a FRET (Fluorescence Resonance Energy Transfer)-based MMP substrate is pre-loaded in the calibration well array and the output well (designated for test sample analysis). The self-calibration capability of the assay establishes a standard curve *in situ* and concurrently with the testing assay, which is particularly useful for mitigating systematic error typically associated with fluorescence spectrometry and ensuring the accuracy of the measurements [44].

The ferrobotic system was programmed to implement the steps of the automated assay within a microfluidic architecture, including 1) sample collection, 2) dispensing (to ensure uniform sample volume), 3) delivery, and 4) merging (with the aid of an electrocoalescence electrode pair) and mixing for sensing (Fig. 5.1b). Specifically, three ferrobots (F_1, F_2, and F_3) were utilized to carry out the required tasks in a pipelined manner. The overview of the navigation plans of the three ferrobots is shown in Fig. 5.1c. In this regard, ferrobot F_1 is in charge of collecting and dispensing the source and test samples into smaller uniform droplets. Ferrobot F_2 is responsible for delivering the dispensed droplets to the designated detection wells, and ferrobot F_3 is tasked with removing the dispensed droplet residues to the waste chamber. The detailed timeline of the task sequence executed by each ferrobot in coordination with the other two ferrobots, along with representative snapshots of the navigation floor status, are illustrated in Fig. 5.1c&d.
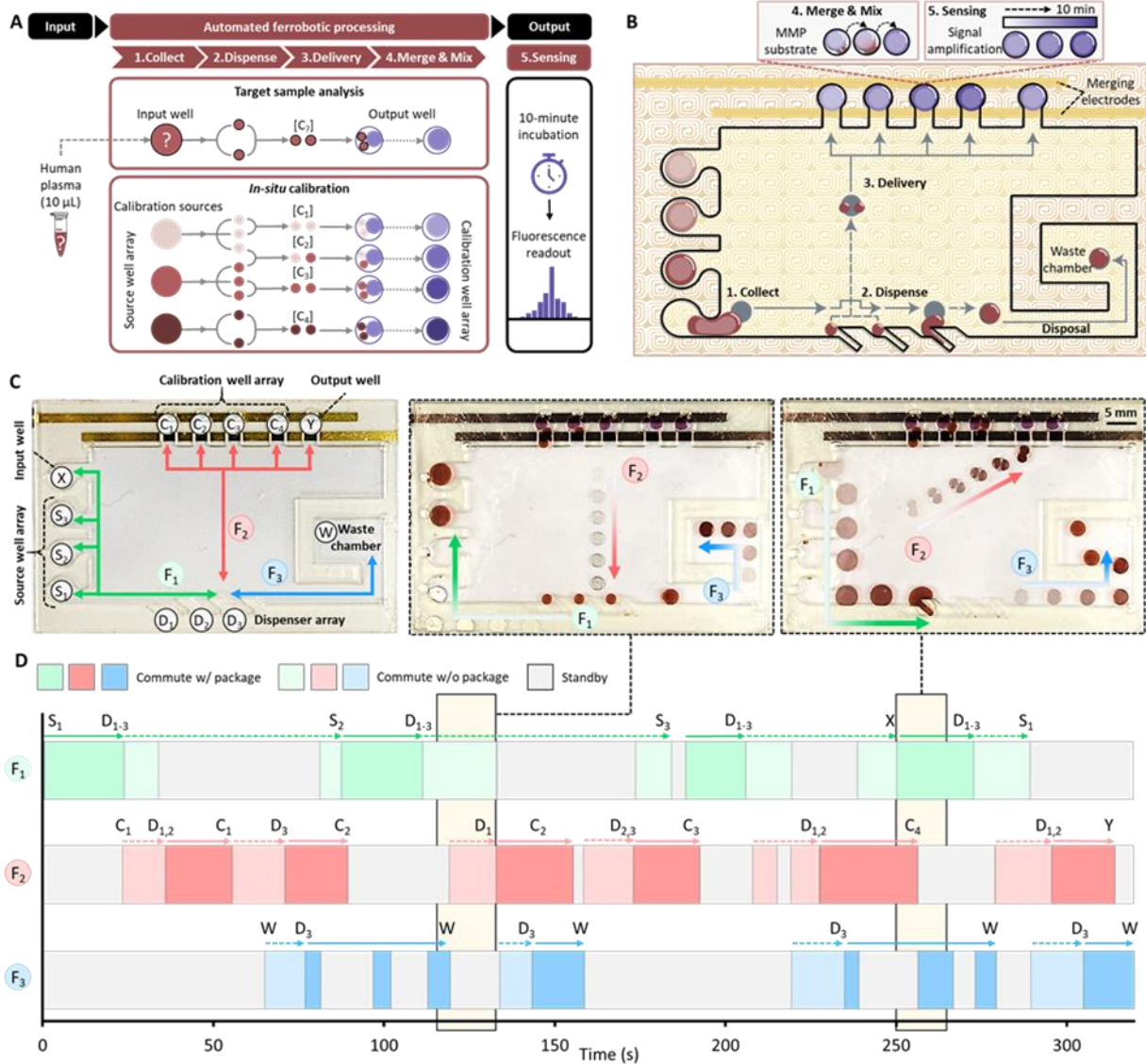
Figure 5.1 *Pipelined and automated MMP assay, performed by the ferrobotic system. a) General workflow of the MMP assay equipped with a dynamic self-calibration mechanism; b) Illustration of the ferrobotic tasks in relation to the navigation floor over the processing of a representative sample (performed by three ferrobots); c) Overview of the navigation plans of the three deployed ferrobots (F1, F2, and F3) with annotated locations of interest; d) The detailed timeline of the ferrobots' status (commuting with/without package, standby), with annotated locations of interest. Overlaid sequential video frames illustrating the status at two representative stages.*

5.2. Evaluation of MMP content in human plasma

Upon delivering the dispensed calibrator/test sample droplets to the calibration well array/output

well, the electrocoalescence electrode pair (a single pair patterned across all the detection wells)

23

is activated, merging the delivered droplets with the pre-loaded MMP substrate within each well all at once. To achieve a homogenous mixture after merging, ferrobot F2 can induce a chaotic internal flow. Upon merging and mixing of the samples with MMP substrate, enzymatic reactions (Fig. 5.2a) effectively commence at the same time, resulting in the generation of fluorescent signal proportional to the respective MMP content in a well. The fluorescent signals are quantitively analyzed by fluorescence microscopy. The linearity of the fluorescent signals with the MMP content of a sample was validated by spiking collagenase in a phosphate-buffered saline (PBS) buffer at different levels and reading out fluorescence after a 10 min incubation (Fig. 5.3). To evaluate the analytical accuracy of the ferrobotic assay for measuring the MMP content in human plasma, four calibrator samples with collagenase concentration of 0.003, 0.006, 0.009, 0.012 Wünsch U/mL were used to determine the MMP concentration of a test sample (human plasma spiked with MMP at a collagenase concentration of 0.008 U/mL). As illustrated in Fig. 5.2b, by referring to the real-time standard curve generated by the calibrator samples, the test sample MMP content was measured to be 0.0078 U/mL ± 0.0005 U/mL (based on 95% confidence interval). To further evaluate the analytical performance of the ferrobotic assay, four additional test samples were analyzed by the ferrobotic system, as well as by a technician using manual pipetting steps and a plate reader [45]. As shown in Fig. 5.2c, the readouts obtained from the ferrobotic system closely matched those analyzed using standard manual analysis ($P < 0.01$), which in turn illustrates the successful execution of all ferrobotic instructions with a high degree of and robustness and precision. This pipelined assay exemplifies the capacity of the ferrobotic system to perform highly quantitative biochemical processes with a high level of integration and automation.
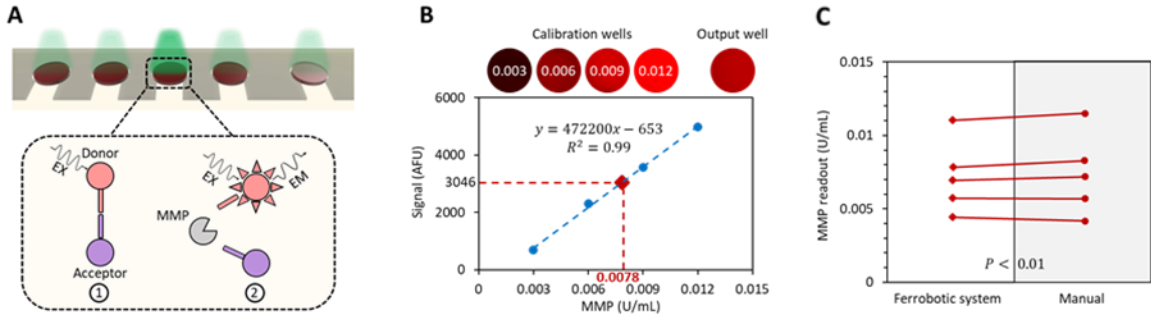
Figure 5.2 *Results of pipelined and automated MMP assay, performed by the ferrobotic system.*
a) Illustration of the FRET pair from the MMP substrate cleaved by the MMPs present in the
sample to yield a fluorescent product that is no longer quenched; b) The fluorescent readouts
from the calibration and output wells, after automated ferrobotic processing and 10 minutes of
incubation. The concentration of MMP in the test sample is estimated with the aid of a real-time
calibration standard curve generated from the 4 calibrator samples (estimated: 0.0078 U/mL vs.
expected: 0.008 U/mL); c) Estimated MMP concentrations in five tested human plasma samples
(performed by the ferrobotic system and manually by a technician, p < 0.01).
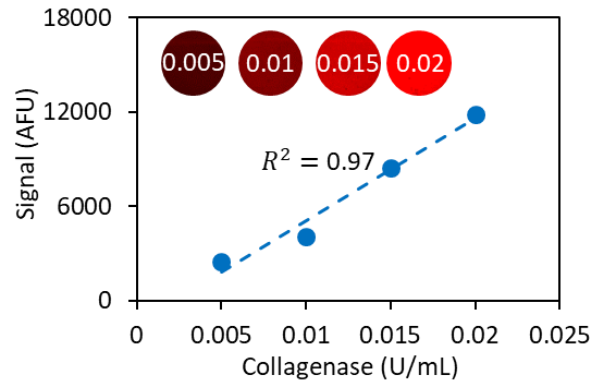
Figure 5.3 *Characterization of the MMP assay. The recorded fluorescence signals from the*
calibration well array, where each well contains PBS dilutions of collagenase at different end
concentrations.

25

Chapter 6　Conclusions and prospects

Inspired by the degrees of freedom achieved by the emergence of AGV robotic systems in terms of mobility and automation, here, for the first time, the concept of a ferrobotic system is introduced and experimentally demonstrated. Accordingly, an amplified addressable electromagnetic actuation mechanism is devised for robotic guidance. The contactless (*i.e.*, no ferrobotic contact with the package or the surrounding fluid) and high-strength actuation mechanism inherently renders it rapid (10 cm/s), repeatable (> 10,000 cycles) and robust (> 24 hours). These traits, together with the reconfigurability of the system, enabled the implementation of advanced and diverse operations through the integration of passive and active functional components. To this end, droplet microfluidic operations, including dispensing, generation, merging, and filtering, were designed and characterized, where the results indicated minimal undesired operational performance deviation. Furthermore, we demonstrated the significantly elevated efficiency of the ferrobotic system for microfluidic logistics applications by deploying a network of cross-collaborative ferrobots to deliver an illustrative and generalizable package sorting objective. To showcase an application where logistics of sample dosing, merging, and mixing are required, we leveraged the advanced and cross-collaborative ferrobotic operations to achieve a pipelined and automated bioassay for the quantification of MMPs in human plasma.

Collectively, our characterization results demonstrate precise, repeatable, durable, and cross-collaborative ferrobotic operations in versatile settings. While these operations were realized with a 32 × 32 addressable navigation floor, the scale of the ferrobotic operations can be expanded by simply adopting a larger navigation floor (requiring minimal reconfiguration of the PCB, specifically, increasing the number of electromagnetic coils). In that regard, augmentation

with image or electrical ferrobot/droplet positioning sensing capabilities within the ferrobotic system allows for the implementation of a feedback control process as a corrective measure to ensure the robustness of desired large-scale operations. Furthermore, the optical readout of the assay is currently performed using a benchtop fluorescence microscope. Further automation and integrated sample-to-answer solutions, especially in point-of-care settings, would benefit from integrated low-cost readers leveraging consumer electronic devices [46]. Alternatively, other assays could be read using electrochemical sensors, which can be integrated onto the platform in a similar manner as the electrodes used for electrocoalescence. Exploiting the ferrofluid biocompatibility [47,48], fluorescence and electrochemical assays can be adapted for applications centering on cell and nucleic acid analysis [49].

On a broader level, adaptation of the ferrobotic system for translational applications necessitates future and convergent designated efforts in microscopic and macroscopic domains toward establishing a generalizable design space for the ferrobotic system. Microfluidic physics-focused efforts are required to comprehensively model the underlying ferrobotic actuation mechanism and understand its limitations in relation to relevant forces, scaling of dimensions (including magnet-, droplet-, and microfluidic structure dimensions), fluidic properties, and other design parameters. Furthermore, macroscopically, dynamic navigation planning algorithms are required to optimize the performance of the cross-collaborative ferrobots toward the delivery of the required objective(s) and in the presence of operational constraints (such as a ferrobotic "safety distance"). To this end, readily developed models from the AGV community aiming to address issues such as layout challenges, fleet management, speed/movement limitations, and optimization functions can be adapted and applied within the framework of the ferrobotic system.

The versatility, scalability, and reconfigurability of the devised ferrobotic system allows for its adaptation to perform diverse and massively parallelized and sequential microfluidic operations relevant to diverse application spaces including point-of-care diagnostics, -omics, drug development, and chemical/material synthesis. By capitalizing on the high degree of automation that can be achieved by the presented technology, large data sets can be generated to unravel complex biological and chemical processes—seeding the transformation of the biotechnology and pharmaceutical industries, mirroring the impact of the AGV robotic systems on their respective industries.

Appendix A: Force balance model of ferrofluid droplet transportation

In our model, three forces are considered to play dominant roles in ferrofluid droplet kinetics: a magnetic body force $\boldsymbol{F}_M$, friction force between the droplet and substrate $\boldsymbol{F}_f$, and drag force on a droplet in an oil environment $\boldsymbol{F}_{drag}$. Here, we ignore droplet deformation by shear because of the low capillary number, which captures the relative strength of viscous forces in the presence of surface tension. Specifically, in our context the capillary number is on the order of 0.002-0.02 (assuming surface tension ~7 mN/m, viscosity of the oil ~1.3 mPa·s, and velocity ~10-100 mm/s). Because of the low capillary number, we also assume the droplet will adopt a minimal surface shape.

The magnetic body force can be expressed as:

$$\boldsymbol{F}_M = \frac{V_M \chi}{\mu_0}(\boldsymbol{B} \cdot \nabla)\boldsymbol{B}$$

where V_M is the magnetically actuated volume of ferrofluid droplet, χ is the magnetic susceptibility (proportional to ferrofluid concentration), μ_0 is permeability of free space, and $\boldsymbol{B}$ is the magnetic flux density.

Friction force between the ferrofluid droplet and substrate of the channel is on the order of:

$$\boldsymbol{F}_f \sim K_f R_b \mu_{oil} U$$

where K_f is the friction constant, R_b is the radius of the contact area between ferrofluid droplet and substrate beneath, μ_{oil} is the viscosity of the oil, and U is the velocity of the carrier (assuming that viscous drag in the vicinity of the contact line is significant).

Given the relatively small value of the Reynold number (Re < 12-120, assuming viscosity of the oil ~1.3 mPa·s, density of the oil ~1614 kg/m^3, characteristic length-scale ~1 mm, and velocity

~10-100 mm/s), and assuming that the droplet motion is in near-steady state, drag force is on the order of:

$$F_{drag} \sim 3\pi D\mu_{oil}U\frac{1 + 2\mu_{oil}/3\mu_{ff}}{1 + \mu_{oil}/\mu_{ff}}$$

where D is the diameter of the droplet and μ_{ff} is the viscosity of the ferrofluid.

During the process of magnetic actuation, F_f and F_{drag} act as restraining forces to counteract the driving force F_M. This net effect can be described as $F_M - F_f - F_{drag} = ma$, where m is the mass of droplet and a is the acceleration of the droplet motion. Accordingly, this relationship sets an upper-bound on the droplet velocity, which can be expressed as:

$$U \leq \frac{\frac{V_M\chi}{\mu_0}(\boldsymbol{B}\cdot\nabla)\boldsymbol{B}}{K_f R_b \mu_{oil} + 3\pi D\mu_{oil}\frac{1 + 2\mu_{oil}/3\mu_{ff}}{1 + \mu_{oil}/\mu_{ff}}} = U_{\max} \quad (1)$$

As equation 1 shows, the concentration related variable (χ) and three size related variables (V_M, R_b, D) affect this velocity limit. Specifically, U_{max} is proportional to magnetic susceptibility χ, illustrating that a higher concentration of ferrofluid results in a larger velocity limit. For size related variables, V_M determines the magnetic actuation force (in the numerator), while R_b and D (in the denominator) affect the friction and drag force respectively. When the volume of ferrofluid droplet (V) is smaller than the characteristic length scale (on the order of the coil size) of the activated EM-field, whole droplet is considered magnetically actuated ($V_M \approx V$). In this case, the increase of V results in the increase of U_{max} because of scaling relations ($V \propto R_b^3 \propto D^3$ isometrically). However, V_M will reach a saturation value when V is considerably larger than the characteristic length scale of the localized EM-field. In this scenario, two restraining forces opposing the droplet movement, F_f and F_{drag}, tend to lower the velocity limit when the carrier volume increases, caused by increasing R_b and D.

References

1. J. Lambert, How Robots Change the World (Oxford Economics, 2019), vol. 43, pp. 5–8.

2. J.-T. Li, H.-L. Liu, Design optimization of amazon robotics. Automat. Contr. Intel. Syst. 4, 48–52 (2016).

3. A. H. C. Ng, R. Fobel, C. Fobel, J. Lamanna, D. G. Rackus, A. Summers, C. Dixon, M. D. M. Dryden, C. Lam, M. Ho, N. S. Mufti, V. Lee, M. A. M. Asri, E. A. Sykes, M. D. Chamberlain, R. Joseph, M. Ope, H. M. Scobie, A. Knipes, P. A. Rota, N. Marano, P. M. Chege, M. Njuguna, R. Nzunza, N. Kisangau, J. Kiogora, M. Karuingi, J. W. Burton, P. Borus, E. Lam, A. R. Wheeler, A digital microfluidic system for serological immunoassays in remote settings. Sci. Transl. Med. 10, eaar6076 (2018).

4. V. Srinivasan, V. K. Pamula, R. B. Fair, An integrated digital microfluidic lab-on-a-chip for clinical diagnostics on human physiological fluids. Lab Chip 4, 310–315 (2004).

5. A. H. C. Ng, M. D. Chamberlain, H. Situ, V. Lee, A. R. Wheeler, Digital microfluidic immunocytochemistry in single cells. Nat. Commun. 6, 7513 (2015).

6. A. R. Wheeler, H. Moon, C. A. Bird, R. R. O. Loo, C.-J. C. J. Kim, J. A. Loo, R. L. Garrell, Digital microfluidics with in-line sample purification for proteomics analyses with MALDI-MS. Anal. Chem. 77, 534–540 (2005).

7. A. Stark, D. J. Shin, T.-H. Wang, A sample-to-answer droplet magnetofluidic assay platform for quantitative methylation-specific PCR. Biomed. Microdevices 20, 31 (2018).

8. A. Stark, D. J. Shin, T.-H. Wang, A sample-to-answer droplet magnetofluidic assay platform for quantitative methylation-specific PCR. Biomed. Microdevices 20, 31 (2018).

9. H. Ding, S. Sadeghi, G. J. Shah, S. Chen, P. Y. Keng, C.-J. C. J. Kim, R. M. van Dam, Accurate dispensing of volatile reagents on demand for chemical reactions in EWOD chips. Lab Chip 12, 3331–3340 (2012).

10. M. Antfolk, T. Laurell, Continuous flow microfluidic separation and processing of rare cells and bioparticles found in blood – A review. Anal. Chim. Acta 965, 9–35 (2017).

11. M. Karle, S. K. Vashist, R. Zengerle, F. von Stetten, Microfluidic solutions enabling continuous processing and monitoring of biological samples: A review. Anal. Chim. Acta 929, 1–22 (2016).

12. D. Di Carlo, D. Irimia, R. G. Tompkins, M. Toner, Continuous inertial focusing, ordering, and separation of particles in microchannels. Proc. Natl. Acad. Sci. U.S.A. 104, 18892–18897 (2007).

13. M. Abdelgawad, A. R. Wheeler, The digital revolution: A new paradigm for microfluidics. Adv. Mater. 21, 920–925 (2009).

14. M. G. Pollack, R. B. Fair, A. D. Shenderov, Electrowetting-based actuation of liquid droplets for microfluidic applications. Appl. Phys. Lett. 77, 1725 (2000).

15. K. Choi, A. H. C. Ng, R. Fobel, A. R. Wheeler, Digital Microfluidics. Annu. Rev. Anal. Chem. 5, 413–440 (2012).

16. M. Mibus, G. Zangari, Performance and reliability of electrowetting-on-dielectric (EWOD) systems based on tantalum oxide. ACS Appl. Mater. Interfaces 9, 42278–42286 (2017).

17. Y. Zhang, N.-T. Nguyen, Magnetic digital microfluidics- A review. Lab Chip 17, 994–1008 (2017).

18. J. Pipper, Y. Zhang, P. Neuzil, T.-M. Hsieh, Clockwork PCR including sample preparation. Angew. Chem. Int. Ed. Engl. 47, 3900–3904 (2008).

19. W. H. Koh, K. S. Lok, N.-T. Nguyen, A digital micro magnetofluidic platform for lab-on-achip applications. J. Fluids Eng. 135, 021302 (2013).

20. U. Lehmann, C. Vandevyver, V. K. Parashar, M. A. M. Gijs, Droplet-based DNA purification in a magnetic lab-on-a-chip. Angew. Chem. Int. Ed. Engl. 45, 3062–3067 (2006).

21. C.-H. Chiou, D. J. Shin, Y. Zhang, T.-H. Wang, Topography-assisted electromagnetic platform for blood-to-PCR in a droplet. Biosens. Bioelectron. 50, 91–99 (2013).

22. M. Egeblad, Z. Werb, New functions for the matrix metalloproteinases in cancer progression. Nat. Rev. Cancer 2, 161–174 (2002).

23. L. Sevenich, J. A. Joyce, Pericellular proteolysis in cancer. Genes Dev. 28, 2331–2347 (2014).

24. W. C. Parks, C. L. Wilson, Y. S. López-Boado, Matrix metalloproteinases as modulators of inflammation and innate immunity. Nat. Rev. Immunol. 4, 617–629 (2004).

25. I. Swyer, R. Fobel, A. R. Wheeler, Velocity saturation in digital microfluidics. Langmuir 35, 5342–5352 (2019).

26. J. Li, N. S. Ha, T. Liu, R. M. vanDam, C.-J. Kim, Ionic-surfactant-mediated electro-dewetting for digital microfluidics. Nature 572, 507–510 (2019).

27. S. Kahkeshani, J. E. Kong, Q. Wei, D. Tseng, O. B. Garner, A. Ozcan, D. Di Carlo, Ferrodrop dose-optimized digital quantification of biomolecules in low-volume samples. Anal. Chem. 90, 8881–8888 (2018).

28. S. Kahkeshani, D. Di Carlo, Drop formation using ferrofluids driven magnetically in a step emulsification device. Lab Chip 16, 2474–2480 (2016).

29. Y. Cheng, X. Ye, Z. Ma, S. Xie, W. Wang, High-throughput and clogging-free microfluidic filtration platform for on-chip cell separation from undiluted whole blood. Biomicrofluidics 10, 014118 (2016).

30. X. Qiu, J. A. Lombardo, T. M. Westerhof, M. Pennell, A. Ng, H. Alshetaiwi, B. M. Luna, E. L. Nelson, K. Kessenbrock, E. E. Hui, J. B. Haun, Microfluidic filter device with nylon mesh membranes efficiently dissociates cell aggregates and digested tissue into single cells. Lab Chip 18, 2776–2786 (2018).

31. B. Bhattacharjee, S. A. Vanapalli, Electrocoalescence based serial dilution of microfluidic droplets. Biomicrofluidics 8, 044111 (2014).

32. R. Tewhey, J. B. Warner, M. Nakano, B. Libby, M. Medkova, P. H. David, S. K. Kotsopoulos, M. L. Samuels, J. B. Hutchison, J. W. Larson, E. J. Topol, M. P. Weiner, O. Harismendy, J. Olson, D. R. Link, K. A. Frazer, Microdroplet-based PCR enrichment for large-scale targeted sequencing. Nat. Biotechnol. 27, 1025–1031 (2009).

33. D. J. Eastburn, A. Sciambi, A. R. Abate, Picoinjection enables digital detection of RNA with droplet rt-PCR. PLOS One. 8, e62961 (2013).

34. A. R. Wheeler, H. Moon, C.-J. Kim, J. A. Loo, R. L. Garrell, Electrowetting-based microfluidics for analysis of peptides and proteins by matrix-assisted laser desorption/ ionization mass spectrometry. Anal. Chem. 76, 4833–4838 (2004).

35. A. H. C. Ng, B. B. Li, M. D. Chamberlain, A. R. Wheeler, Digital microfluidic cell culture. Annu. Rev. Biomed. Eng. 17, 91–112 (2015).

36. R. Cole, Parallel merge sort. SIAM J. Comput. 17, 770–785 (1988)

37. M. Dhar, J. N. Lam, T. Walser, S. M. Dubinett, M. B. Rettig, D. Di Carlo, Functional profiling of circulating tumor cells with an integrated vortex capture and single-cell protease activity assay. Proc. Natl. Acad. Sci. U.S.A. 115, 9986–9991 (2018).

38. R. E. Vandenbroucke, L. Dejager, C. Libert, The first MMP in sepsis. EMBO Mol. Med. 3, 367–369 (2011).

39. G. Martin, V. Asensi, A. H. Montes, J. Collazos, V. Alvarez, J. A. Carton, F. Taboada, E. Valle-Garay, Role of plasma matrix-metalloproteases (MMPs) and their polymorphisms (SNPs) in sepsis development and outcome in ICU patients. Sci. Rep. 4, 5002 (2014).

40. I. Vanlaere, C. Libert, Matrix metalloproteinases as drug targets in infections caused by gram-negative bacteria and in septic shock. Clin. Microbiol. Rev. 22, 224–239 (2009).

41. L. Nissinen, V.-M. Kähäri, Matrix metalloproteinases in inflammation. Biochim. Biophys. Acta. 1840, 2571–2580 (2014).

42. L. Ravanti, V. M. Kähäri, Matrix metalloproteinases in wound repair (review). Int. J. Mol. Med. 6, 391–407 (2000).

43. A. Gutiérrez-Fernández, M. Inada, M. Balbín, A. Fueyo, A. S. Pitiot, A. Astudillo, K. Hirose, M. Hirata, S. D. Shapiro, A. Noël, Z. Werb, S. M. Krane, C. López-Otín, X. S. Puente, Increased inflammation delays wound healing in mice deficient in collagenase-2 (MMP-8). FASEB J. 21, 2580–2591 (2007).

44. E. M. Miller, A. R. Wheeler, A Digital microfluidic approach to homogeneous enzyme assays. Anal. Chem. 80, 1614–1619 (2008).

45. D. H. Nam, X. Ge, Development of a periplasmic FRET screening method for protease inhibitory antibodies. Biotechnol. Bioeng. 110, 2856–2864 (2013).